BIOCHEMISTRY
including biophysical chemistry & molecular biology

Article

pubs.acs.org/biochemistry

The First Residue of the PWWP Motif Modulates HATH Domain Binding, Stability, and Protein−Protein Interaction

Yi-Lin Hung,[†] Hsia-Ju Lee,[†] Ingjye Jiang,[†] Shang-Chi Lin,[†] Wei-Cheng Lo,[§] Yi-Jan Lin,[∥] and Shih-Che Sue*[,†,‡]

[†]Institute of Bioinformatics and Structural Biology and [‡]Department of Life Science, National Tsing Hua University, Hsinchu, Taiwan

[§]Institute of Bioinformatics and Structural Biology, National Chiao Tung University, Hsinchu, Taiwan

[∥]Graduate Institute of Natural Products and Center of Excellence for Environmental Medicine, Kaohsiung Medical University, Kaohsiung, Taiwan

Supporting Information

ABSTRACT: Hepatoma-derived growth factor (hHDGF) and HDGF-related proteins (HRPs) contain conserved N-terminal HATH domains with a characteristic structural motif, namely the PWWP motif. The HATH domain has attracted attention because of its ability to bind with heparin/heparan sulfate, DNA, and methylated histone peptide. Depending on the sequence of the PWWP motif, HRP HATHs are classified into P-type (Pro-His-Trp-Pro) and A-type (Ala-His-Trp-Pro) forms. A-type HATH is highly unstable and tends to precipitate in solution. We replaced the Pro residue in P-type $HATH_{HDGF}$ with Ala and evaluated the influence on structure, dynamics, and ligand binding. Nuclear magnetic resonance (NMR) hydrogen/deuterium exchange and circular dichroism (CD) measurements revealed reduced stability. Analysis of NMR backbone ^{15}N relaxations (R_1, R_2, and nuclear Overhauser effect) revealed additional backbone dynamics in the interface between the β-barrel and the C-terminal helix bundle. The $\beta1-\beta2$ loop, where the AHWP sequence is located, has great structural flexibility, which aids HATH−HATH interaction through the loop. A-type HATH, therefore, shows a stronger tendency to aggregate when binding with heparin and DNA oligomers. This study defines the role of the first residue of the PWWP motif in modulating HATH domain stability and oligomer formation in binding.

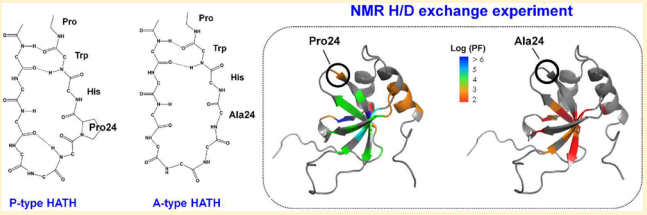

The PWWP domain is a weakly conserved structural module named for its signature Pro-Trp-Trp-Pro motif.[1] The domain consists of 100−150 amino acids and is found in a number of eukaryotic proteins that are involved in cell division, growth, and differentiation.[2] The PWWP domain was first identified as a structural motif in the Wolf−Hirschhorn syndrome critical region proteins (WHSC1)[1,3] and further studied in hepatoma-derived growth factor (HDGF).[4−6] On the basis of sequence homology, the PWWP domains have been categorized into several classes,[2] and more than 10 structures of the PWWP domains have been determined in recent years[7] since the first structure was determined for the DNA methyltransferase DNMT3B.[8] These PWWP domains consist of a five-stranded antiparallel β-barrel and an α-helix bundle in their C-termini, and the PWWP motif is located in the N-terminal part of $\beta2$.[9] Among these four residues, the first and second residues exhibit variation, and only the third (Trp) and fourth (Pro) residues are highly conserved.[7]

The PWWP domain has been reported to play distinct roles on both sides of the cell membrane.[10−12] However, the exact biological function of the PWWP domain remains controversial and has not yet been established. Three interacting partners have been commonly addressed, namely, methylated histone, DNA, and heparin/heparan sulfate.[5,6,13,14] Methylated histone peptide has been reported to weakly bind a highly conserved hydrophobic cage on the PWWP domain surface, constituted by three aromatic residues: the Tyr/Phe residue before the PWWP motif, the third residue (Trp) of the PWWP motif, and another aromatic residue (Phe/Trp/His) in $\beta3$.[15,16] Many PWWP domains have DNA binding ability, allowing some proteins to behave as transcription factors in regulating a variety of developmental processes.[17−19] PWWP domains contain a characteristic electrostatic surface where conserved positively charged residues are clustered in a polarized patch next to the hydrophobic cage.[20] The charged patch is responsible for binding both DNA and heparin.[4,5] Thus, the combination of the two binding sites provides the possible mechanism of chromatin binding in which the conserved hydrophobic cage anchors the methylated histone molecule, and the charged patch makes contact with the nucleic acid.[13,21−23] However, the PWWP DNA binding is nonspecific.[6] There is still no structure for the PWWP−DNA−methylated peptide ternary complex or even the PWWP−DNA complex.

We align the sequences of the PWWP domains with all available structures, including BRPFs, DNMT3A, DNMT3B,

Received: April 24, 2015
Revised: June 11, 2015
Published: June 11, 2015

DOI: 10.1021/acs.biochem.5b00454
Biochemistry 2015, 54, 4063−4074

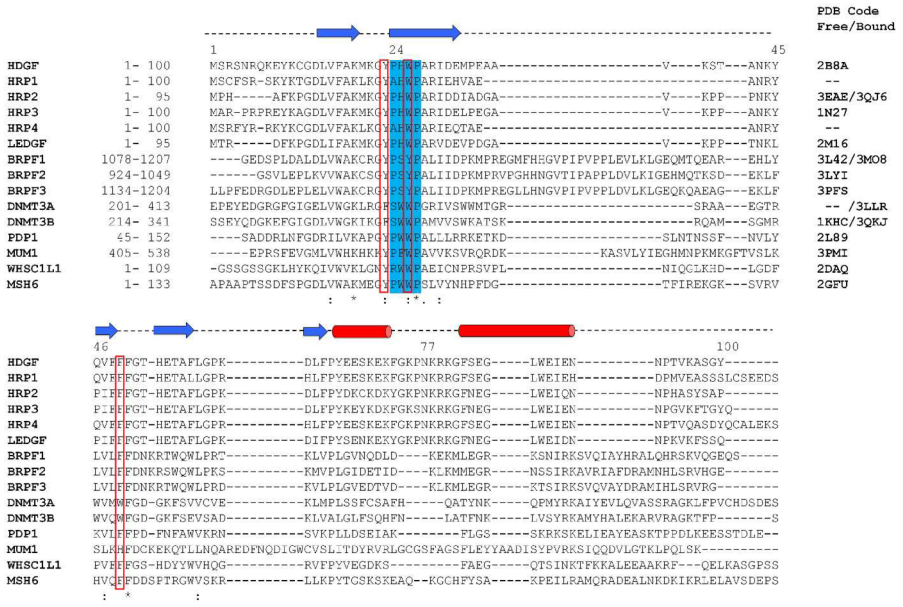

Figure 1. Multiple-sequence alignments of the PWWP domains of various PWWP-containing proteins. HDGF-related protein: HDGF, HRP1, HRP2, HRP3, HRP4, and LEDGF. Bromo domain- and PHD finger-containing protein: BRPF1, BRPF2, and BRPF3. DNA methyltransferase: DNMT3A and DNMT3B. *Schizosaccharomyces pombe* PWWP domain-containing protein: PDP1. Mutated melanoma-associated antigen 1: MUM1. Wolf-Hirschhorn syndrome critical region: WHSC1L1. Mismatch repair protein: MSH6. The secondary structure elements of the HDGF PWWP domain ($HATH_{HDGF}$) are shown above the alignments, with arrows representing β-strands and cylinders representing α-helices. The PWWP motif is highlighted in blue, and the residues constituting the aromatic cage are boxed in red. The alignment was generated using Clustal Omega with manual adjustment.

PDP1, MUM1, WHSC1L1, and MSH6, along with HDGF-related proteins (HRPs) (Figure 1). As described, among the determined structures, the first and second residues of the PWWP motif show variation. Pro is primarily found as the first residue, and the other examples are Ser or Arg residues. The first residue of the PWWP motif, located at the end of the $\beta1-\beta2$ loop, has a solvent-accessible side chain. Via comparison of the PWWP motifs in the six mammalian HRPs, there are two types of sequences. PHWP appears in HDGF, HRP2, HRP3, and lens epithelium-derived growth factor (LEDGF) and AHWP in HRP1 and HRP4 (Figure 1).[24] Interestingly, these P-type HRP PWWP domains have available structures, whereas the structural determination of A-type HRP PWWP domains has failed in our experience. The A-type PWWP domains exhibited structural instability and protein precipitation, which impeded the determination of their structures. No study has thus far addressed the roles of the individual residues of the PWWP motif. We cannot know whether this single-residue difference could cause this structural instability. It will be of great value to see how the sequence variation in the PWWP domain changes the structural properties. The HRP family provides an excellent model for evaluating the consequences of changing the first residue of the PWWP motif.

HRPs play dual roles on both sides of the plasma membrane by either binding to DNA in the nucleus as a transcriptional factor or interacting with membrane surface carbohydrates as a growth factor.[11,25−28] They were classified on the basis of the conserved N-terminal PWWP domain, usually called the HATH (homologous to the amino terminus of HDGF) domain.[6,9] Recent studies have confirmed the consensus role of HATHs in binding heparin, DNA, and methylated peptides,[4−6,14,15,18] whereas the functions of HRP C-terminal domains with different lengths and charges remain unknown.[4] Different cellular effects have been reported for different HRPs. HDGF is a mitogenic, tumorigenic, and angiogenic factor *in vivo*.[27,29] HRP3 acts as a neurotrophic and neurite outgrowth-promoting factor by interacting with microtubules.[30] LEDGF has been identified as a HIV-1 integrase-binding protein.[15,28,31] In addition, HRPs have notable value as prognostic factors in several types of cancers.[26,32−34]

In light of the diverse functions of HRPs, research focusing on the PWWP sequence could establish the structure−function relationships for individual HATHs and meanwhile provide a common understanding of the importance of the PWWP motif in maintaining the structural fold. Here, we employ nuclear magnetic resonance (NMR) to compare the structural and dynamic differences between the P- and A-type HATHs. The results indicate the crucial role of the first residue of the PWWP motif in modulating the $\beta1-\beta2$ loop structure and domain stability. In addition, A-type HATH has lower structural stability and exhibits a stronger preference for aggregation when binding polymer ligands.

MATERIALS AND METHODS

HATH Constructs and Site-Directed Mutagenesis. The cloning, expression, and purification of HRP HATHs have been described previously.[4,5] In short, the coding regions of HRP HATHs corresponding to HDGF HATH 1−100 ($HATH_{HDGF}$) and HRP4 HATH 1−100 ($HATH_{HRP4}$) were amplified by polymerase chain reaction (PCR) and inserted into a pET-6H expression vector. Two point mutations, $HATH_{HDGF}$ P24A and $HATH_{HRP4}$ A23P, were prepared through a standard procedure of site-directed mutagenesis, using the pET6H-HATH plasmid as a template. All constructed plasmids were verified by DNA sequencing.

Expression and Purification of HATH Domains. *Escherichia coli* strain BL21(DE3) was used to express various HATHs. The expressed HATHs contain a hexahistidine tag at

DOI: 10.1021/acs.biochem.5b00454
Biochemistry 2015, 54, 4063−4074

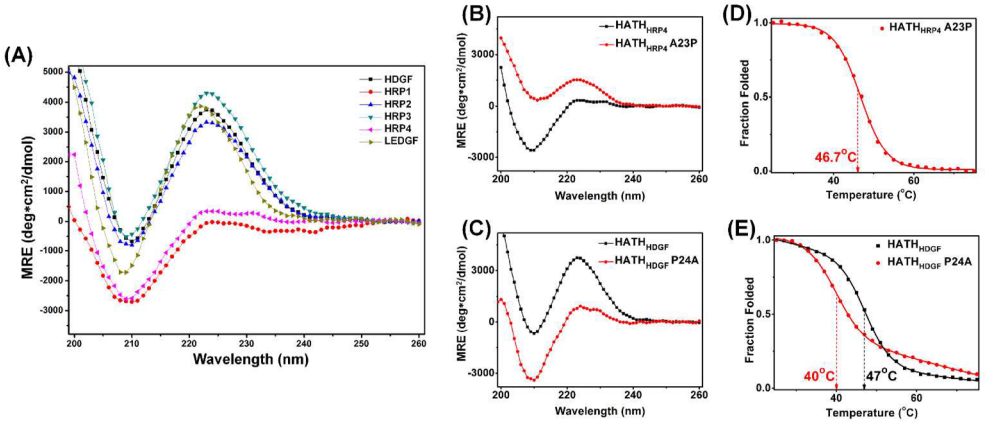

Figure 2. Far-UV CD spectra of HRP HATHs. (A) CD spectra of the six mammalian HRP HATHs at 25 °C. (B) Comparison of far-UV CD spectra of recombinant $HATH_{HRP4}$ and the A23P mutant. (C) Comparison of far-UV CD spectra of $HATH_{HDGF}$ and the P24A mutant. (D) Thermal denaturation curve of $HATH_{HRP4}$ A23P monitored at a wavelength of 224 nm. (E) Thermal denaturation curves of $HATH_{HDGF}$ and $HATH_{HDGF}$ P24A.

their N-termini for rapid purification. Cells harboring one of the expression vectors were grown in LB medium with 0.1 mg/mL ampicillin at 37 °C and subsequently induced with 1 mM isopropyl β-D-1-thiogalactopyranoside (IPTG) when the OD_{600} value reached 0.6. After another 4 h induction at 37 °C for HATHs and a 16 h induction at 24 °C for $HATH_{HDGF}$ P24A and $HATH_{HRP4}$, the cells were harvested by centrifugation and kept frozen at −20 °C before being purified. The harvested cells were resuspended in lysis buffer [50 mM sodium phosphate buffer (pH 8.0), 300 mM NaCl, and 10 mM imidazole] and ruptured by a high-pressure homogenizer (Impact Mixer, GW Technologies, Taiwan). The soluble HATHs in the supernatant were purified using a column packed with Ni-charged resin (GE Healthcare) and eluted by the same buffer except containing 250 mM imidazole. To enhance protein stability, 5% glycerol was added to purify $HATH_{HRP4}$. All HATHs were further purified to homogeneity by size exclusion chromatography using a Superdex 75 column (GE Healthcare) in 50 mM sodium phosphate buffer (pH 7.4), 150 mM NaCl, 1 mM EDTA, and 20 mM β-mercaptoethanol (β-ME). The purified proteins were confirmed by mass spectrometry. The concentrations were estimated on the basis of the extinction coefficient and absorption at 280 nm via a Nanophotometer (IMPLEN). For the preparation of the ^{15}N-labeled or ^{15}N- and ^{13}C-labeled samples for NMR study, the cells were grown in M9 minimal medium supplemented with $^{15}NH_4Cl$ (1 g/L) and [^{13}C]-D-glucose (2 g/L). The labeled protein was purified following the same procedure.

Circular Dichroism (CD). The secondary structure and thermally induced denaturation of HATHs were evaluated by CD spectroscopy using an AVIV 202 spectropolarimeter (AVIV Biomedical, Lakewood, NJ). A sample containing 20 μM HATH in 10 mM phosphate buffer (pH 7.4) and 10 mM NaCl was measured between 190 and 260 nm at 25 °C. To compare optical activity, all spectra were averaged over three scans and converted to mean residue ellipticity (MRE, degrees per square centimeter per decimole). The thermal stability was monitored by the ellipticity change at 224 nm with gradient temperature from 25 to 95 °C, with an increment of 1 °C and a heating rate of 1 °C/min. The fraction of folding is defined as $(\theta_t - \theta_U)/(\theta_F - \theta_U)$, where θ_t is the observed ellipticity at a given temperature and θ_F and θ_U are the values for the folded state and unfolded state, respectively. θ_F and θ_U were obtained by fitting the thermal denaturation curve by a sigmoid function.

NMR HSQC Titration Experiments. Samples containing ~0.5 mM proteins in NMR buffer [10 mM phosphate buffer (pH 6.0), 150 mM NaCl, 10 mM β-ME, and 1 mM EDTA in a 90% H_2O/10% D_2O mixture] were prepared for NMR measurements. We established backbone assignments of $HATH_{HDGF}$ P24A for the resonances of HN, ^{15}N, $^{13}C\alpha$, $^{13}C\beta$, and ^{13}CO via the $^{1}H-^{15}N$ HSQC, HNCA, HN(CO)CA, HN(CA)CB, HN(COCA)CB, and HNCO spectra. All spectra were processed in NMRpipe[35] and analyzed in Sparky.[36] The ^{1}H chemical shift was calibrated using 2,2-dimethyl-2-silapentane-5-sulfonate (DSS) at 0 ppm, and the ^{15}N and ^{13}C chemical shifts were calibrated indirectly using DSS through gyromagnetic ratios. We performed the binding experiments by titrating heparin oligosaccharide, methylated peptide, or DNA fragment into a HATH solution. The heparin-derived oligosaccharides were depolymerized from heparin sodium (H3393, Sigma-Aldrich) as described previously.[5] The N-methylated peptide H3K36me3 [H-Pro-Ala-Thr-Gly-Gly-Val-Lys(me3)-Lys-Pro-His-Arg-Tyr-OH] with three methyl groups and its unmodified counterpart H3K36 (H-Pro-Ala-Thr-Gly-Gly-Val-Lys-Lys-Pro-His-Arg-Tyr-OH)[7] were purchased from Kelowna International Scientific, Inc. The DNA-binding sequence is based on a previous study: a 25 bp double-stranded DNA (5′-CTC CTG ACC TCA GAT GAT CCA TGT G-3′) and a 37 bp double-stranded DNA (5′-CTT GAA CTC CTG ACC TCA GAT GAT CCA TGT GCC TCG G-3′) were synthesized.[18] The integrated DNA chemical shift differences and perturbations induced by these ligands were represented by a combined chemical shift change, $\Delta\delta_{NH+N}$, with $\Delta\delta_{NH+N} = [(\Delta\delta_{NH}^2 + \Delta\delta_N^2/25)/2]^{1/2}$, where $\Delta\delta_{NH}$ and $\Delta\delta_N$ are the chemical shift changes of the backbone amide proton (NH) and the amide (N), respectively.

NMR Relaxation Measurements. Measurements of T_1 and T_2 relaxations and the $[^{1}H]-^{15}N$ heteronuclear nuclear Overhauser effect (NOE) were performed at 25 °C on a Bruker DRX600 instrument. T_1 delays of 10, 50, 100, 200, 400, 600, 800, 1000, 1200, and 1500 ms were used with repeated 50, 400, and 1200 ms; T_2 delays of 0, 17, 34, 51, 68, 102, 136, 170, 204, and 238 ms were used with repeated 34, 102, and 204 ms. For the $[^{1}H]-^{15}N$ NOE measurements, independent saturated and unsaturated spectra were recorded in an interleaved manner.

DOI: 10.1021/acs.biochem.5b00454
Biochemistry 2015, 54, 4063−4074

The spectral data were processed using NMRPipe[35] and Sparky.[36] The ^{15}N R_1 ($1/T_1$) and R_2 ($1/T_2$) relaxation values were analyzed by fitting the series of peak intensity with an exponential decay curve in Sparky. The NOE data were obtained by calculating the peak intensity ratio between the saturated and unsaturated NOE spectra. The relaxation parameters R_1, R_2, and NOE with error values were fitted to model-free equations using FastModelFree.[37] The rotational diffusion tensors, including the D_{ratio} and θ/ϕ angle, were estimated using the R_2/R_1 diffusion programs[38] and pdbinertia (from A. G. Palmer's group).[39] The default values of the N−H bond lengths and ^{15}N chemical shift anisotropy were 1.02 Å and −160 ppm, respectively.[40] The correlation time was initially set to 10 ns during the 25 loops of calculations to fit the five models using model-free formalism.[41,42]

H/D Exchange Experiments. Hydrogen−deuterium exchange experiments were conducted on a Bruker DRX600 instrument at 25 °C. H_2O buffer was rapidly replaced with 100% D_2O buffer using a PD Minitrap G-25 column (GE Healthcare). A series of $^1H-^{15}N$ HSQC spectra were acquired every 18 min during a total exchange time of 18 h. The first experiment was started within 15 min of buffer exchange. Protection factors (PFs) were further determined by calculating the k_{int}/k_{ex} ratio, where k_{ex} is the exchange rate constant determined by fitting a single-exponential function to the amine peak intensities in the series of HSQCs and k_{int} is the intrinsic exchange rate constant estimated from the web server, SPHERE, which corrects for temperature and pH effects.[42]

RESULTS

Thermal Stability. We evaluate whether the stability difference between P- and A-type HATH is derived from the difference in the first residue of the PWWP motif. We compared the CD spectra of all HRP HATHs (Figure 2A). The spectra of P-type HATHs (HDGF, HRP2, HRP3, and LEDGF) gave similar profiles with significant positive ellipticities at 222 nm, representing a well-folded β-barrel structure. A-type HATHs (HRP1 and HRP4), however, exhibit very low ellipticity at the corresponding wavelength. We mutated A23 to Pro in $HATH_{HRP4}$ and P24 to Ala in $HATH_{HDGF}$, where A23 in $HATH_{HRP4}$ corresponds to P24 in $HATH_{HDGF}$ on the basis of the sequence alignment (Figure 1). The $HATH_{HRP4}$ A23P mutant showed a CD profile more similar to the results for the P-type HATHs (Figure 2B). The $HATH_{HDGF}$ P24A mutant behaved as an A-type HATH (Figure 2C). Wild-type $HATH_{HRP4}$ is highly unstable and precipitated when the temperature was increased. It was only possible to determine the melting temperature (T_m) of the $HATH_{HRP4}$ A23P mutant, at 46.7 °C (Figure 2D). $HATH_{HDGF}$ is more stable than the P24A mutant, and the T_m values for the wild type and P24A are 47 and 40 °C, respectively (Figure 2E). Notably, P24A did not exhibit a typical two-state transition during the thermally induced denaturation, indicating a lower structural cooperativity. These single mutations swapped the structural properties of P- and A-type HATHs. Thus, the first residue of the PWWP motif determines HATH secondary structure and stability.

NMR HSQC Comparison of Wild-Type $HATH_{HDGF}$ and the P24A Mutant. To compare A-type and P-type HATHs, we chose $HATH_{HDGF}$ as a model to clarify the influence derived from the first residue of the PWWP motif. To simplify the description, the notation HATH will be used to represent $HATH_{HDGF}$ in the following discussion, whereas P24A will denote $HATH_{HDGF}$ P24A. The conformational difference between HATH and P24A is first revealed by the comparison of HSQC spectra (Figure 3A). We calculated the combined

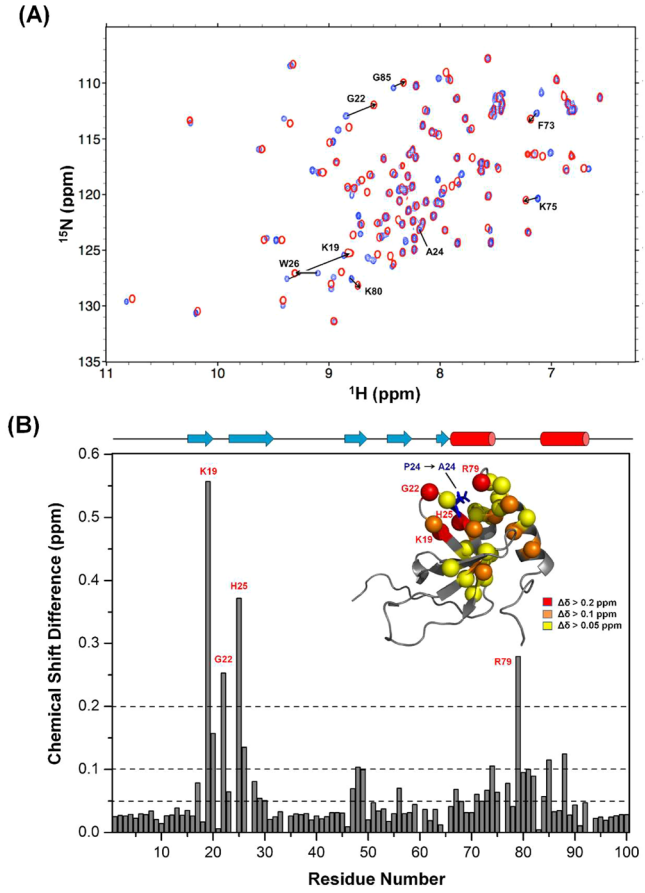

Figure 3. Chemical shift difference between $HATH_{HDGF}$ and $HATH_{HDGF}$ P24A mutant. (A) Overlap of the $^1H-^{15}N$ HSQC spectra of $HATH_{HDGF}$ (blue) and $HATH_{HDGF}$ P24A (red). (B) Combined chemical shift difference of the two proteins. The difference is mapped on the $HATH_{HDGF}$ structure (Protein Data Bank entry 2B8A), and the extent of chemical shift change is indicated by different colors: red, orange, and yellow from large to small scale, respectively.

chemical shift differences and mapped them onto the HATH structure (Figure 3B). The significant conformational differences were widely distributed in the $\beta1-\beta2$ and $\alpha1-\alpha2$ regions. Residues K19, G22, H25, and R79, which lie spatially close to the mutation site, showed the most significant changes ($\Delta\delta$ > 0.2 ppm) (Figure 3B). Residues M20, W26, F48, F49, G74, G85, and E88 with moderate perturbations are distributed at the interface between the β-barrel and the C-terminal helix region.

Secondary structure and backbone conformation analysis. The backbone chemical shifts of $^{13}C_\alpha$ and $^{13}C_\beta$ are sensitive to the backbone dihedral angles. The chemical shift difference between ΔC_α and ΔC_β, derived from $^{13}C_\alpha$ and $^{13}C_\beta$ minus the corresponding random coil values, is usually used as protein secondary structure reporting parameter, where positive and negative values of (ΔC_α-ΔC_β) represent α-helix and β-sheet conformations, respectively. The (ΔC_α-ΔC_β) values of wild-type HATH and P24A are plotted as a function of residue number in Figure 4A and 4B, and the profiles of the two proteins are generally similar, indicating similar secondary structures. To show greater detail, we have plotted $\Delta(\Delta C_\alpha$-

DOI: 10.1021/acs.biochem.5b00454
Biochemistry 2015, 54, 4063−4074

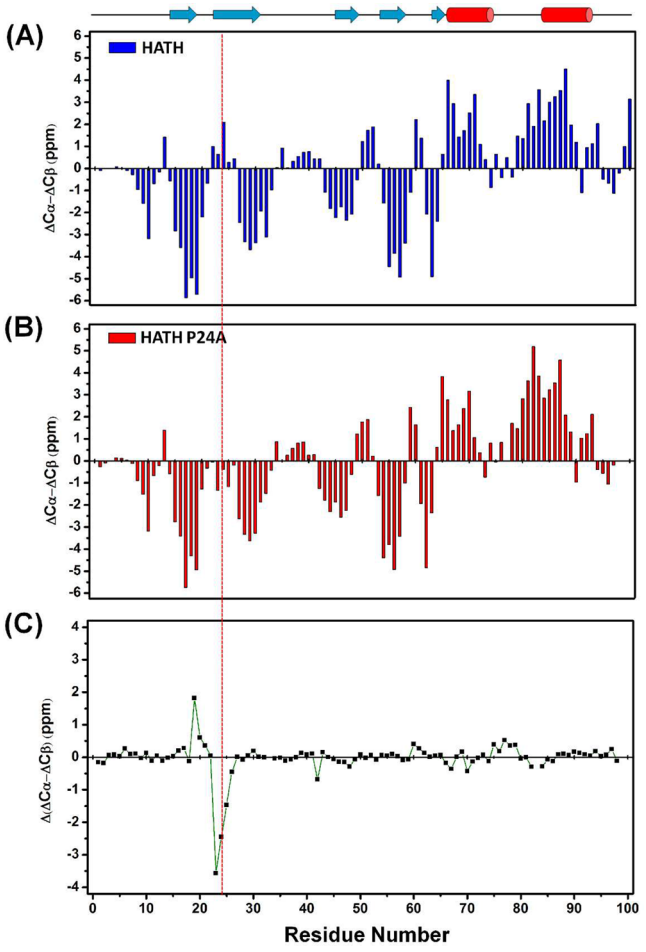

Figure 4. Comparison of secondary structures between $HATH_{HDGF}$ and the P24A mutant. Secondary structure of (A) $HATH_{HDGF}$ and (B) $HATH_{HDGF}$ P24A, predicted by differences in $(\Delta C_\alpha\text{-}\Delta C_\beta)$ values: $(\Delta C_\alpha\text{-}\Delta C_\beta) > 0$ for α-helix and $(\Delta C_\alpha\text{-}\Delta C_\beta) < 0$ for β-sheet. We estimated the value of $\Delta C_\alpha\text{-}\Delta C_\beta$ by averaging three consecutive residues centered at a particular residue. The secondary structure elements of $HATH_{HDGF}$ are shown at the top for comparison. (C) The parameter $\Delta(\Delta C_\alpha\text{-}\Delta C_\beta)$ indicates the secondary structural difference between $HATH_{HDGF}$ and the P24A mutant.

ΔC_β) in Figure 4C, where the value is the difference between HATH and P24A. The mutation caused significant differences in the region surrounding the P24 site. The values of $\Delta(\Delta C_\alpha\text{-}\Delta C_\beta)$ became positive in $\beta1/\beta2$ loop and negative near the mutation site (Figure 4C) that the tendency of β-sheet structure decreased in $\beta1/\beta2$ loop but increased in the mutation site. The region starting from $\beta1/\beta2$ loop to PWWP motif adopts different backbone conformation in the mutant P24A.

NMR Hydrogen−Deuterium (H/D) Exchange Measurements. To obtain information on the local flexibility of HATH and P24A, we used NMR to detect H/D exchange, which provides direct site-specific information on the rate of exchange between amide protons and deuterium in the D_2O solvent. Series of HSQC spectra were acquired at increasing intervals after solvent exchange (Figure 5A). We analyzed the H/D exchange data in term of protection factors (PF). Slow H/D exchanges are reflected by high PF values, representing a higher degree of protection. The results are summarized in Figure 5B and shown on the structures by colors corresponding to different log (PF) values (Figure 5C).The core region of the HATH β-barrel is well protected, and the C-terminal $\alpha2$ region is also stable. The residues with secondary structure have log (PF) values between 3 and 7. The short $\alpha1$ helix is unstable that the resonances were missing in the first HSQC spectrum. In the P24A mutant, only several residues located in the central core of the β-barrel remained detectable, with log (PF) values between 2 and 3 (Figure 5B). The replacement of Pro with Ala at residue 24 disrupts domain stability in both the β-barrel and the C-terminal helices, whereas wild-type HATH exhibits stronger backbone amide protection.

NMR ^{15}N relaxation data. The NMR ^{15}Nrelaxation data on HATH and P24A, including R_1, R_2, and heteronuclear NOEs, were obtained at 600.13 MHz (Figure 6). The R_1, R_2 and NOE experiments are sensitive to protein backbone motion on a ps-ns time scale. After excluding some overlapping resonances, we analyzed 85 of the possible 93 resonances in HATH and P24A. The numerical values of the relaxation data of the two molecules are shown in Figure 6A and 6D. For HATH residues located in the secondary structures, the rates are distributed around the average values, indicating that this portion of the molecule is relatively rigid on the ps-ns time scale (Figure 6A). Meanwhile, the residues located in the N and C-terminus have negative NOEs, and the residues in the loops show reduced NOE values, indicating dynamic properties. The relaxation data collected at P24A are similar, but more scattered values are observed in the R_2 experiment and higher errors in the NOE measurement. The rotational diffusion tensors of HATH and P24A were both estimated from the HATH structure [Protein Data Bank (PDB) entry 2B8A]. The D_{ratio} values of the axially symmetric models of HATH and P24A were 1.22 and 1.24, respectively, and the θ/ϕ angles were 1.2/3.0 and 1.4/2.3 with respect to the molecular axes. The mean relaxation parameters of these resolved amide nitrogens are as follows: in HATH, $R_1 = 1.41 \pm 0.04$ s^{-1} and $R_2 = 11.72 \pm 0.15$ s^{-1}, and in P24A, $R_1 = 1.42 \pm 0.05$ s^{-1} and $R_2 = 11.72 \pm 0.42$ s^{-1}. Therefore, the overall rotational correlation times of HATH and P24A were estimated from the parameter R_2/R_1, with comparable values of 9.6 and 9.4 ns.

FastModelFree Analysis. To obtain precise protein dynamics information, we analyzed the data using FastModelFree fitting. Three dynamics parameters were derived, namely, S^2, T_e, and R_{ex}, representing the order parameter, backbone internal motion, and chemical exchange, respectively (Figure 6B,E). We noticed that most portions of HATH and P24A share similar profiles. Both molecules exhibit rigidity, with S^2 values generally higher than 0.9. The N- and C-terminal regions and the long loop (residue 35−45) have regional flexibility with reduced S^2 and T_e values. Interestingly, the mutation site at residue 24 and the regions centered at residues 58 and 77 show reduced S^2 values and an observable T_e in P24A (Figure 6E). These sites represent regions that exhibit greater structural fluctuation in the P24A mutant. Meanwhile, more residues in P24A exhibit R_{ex}, namely, residues 12, 19, 20, 26, 51, 59, 68, 72, 73, 80, 81, 90, and 94, whereas R_{ex} appears in HATH at residues 12, 23, 62, 81, and 95. These additional residues are distributed spatially near the PWWP motif, indicating the presence of chemical exchange in the local region. We have mapped dynamics parameters S^2 and R_{ex} on the HATH structure (Figure 6C,F). The dynamic sites cover the PWWP motif, the $\beta1-\beta2$ loop, $\beta4$, and the $\alpha1-\alpha2$ region. The P24A mutation creates structural instability in the local region of the PWWP motif and perturbs the proximate regions.

DOI: 10.1021/acs.biochem.5b00454
Biochemistry 2015, 54, 4063−4074

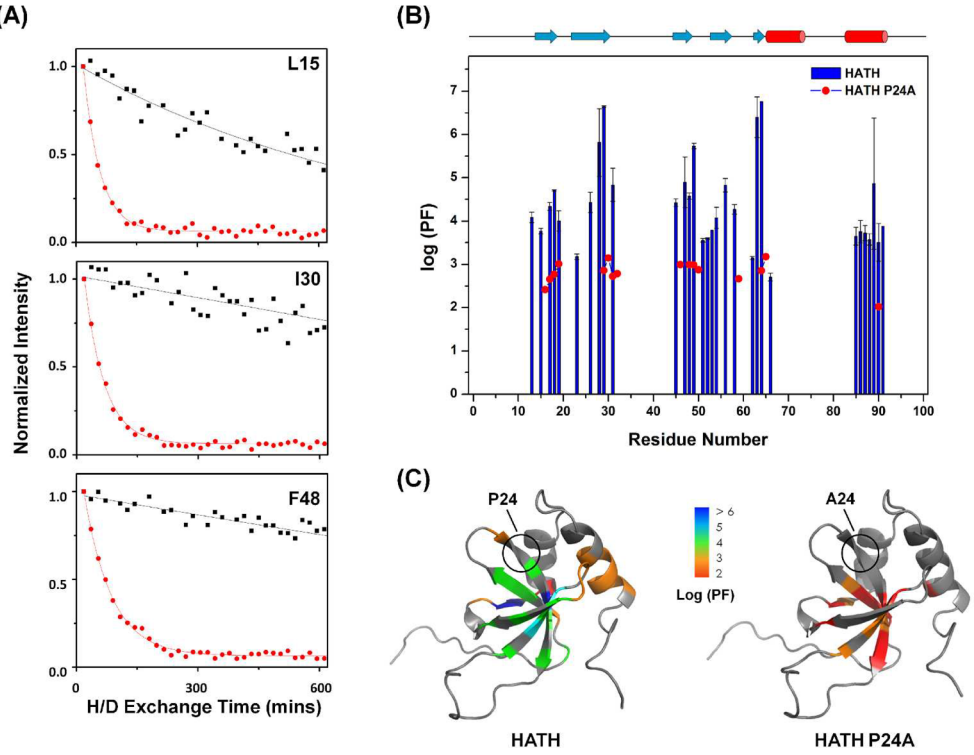

Figure 5. NMR H/D exchange experiment for backbone amides. (A) H/D exchange curves of representative residues of L15, I30 and F48 of $HATH_{HDGF}$ (black squares) and the P24A mutant (red circles). (B) Protection factors of HATHs derived from the $^{1}H-^{15}N$ HSQC H/D exchange experiment. (C) The protected residues are mapped on the HATH structure with different colors according to the corresponding log (PF) values.

Chemical Shift Difference in Ligand Titration. We titrated the three HDGF-binding targets into HATH and P24A solutions. The titration-induced chemical shift changes, $\Delta\delta_{NH+N}$, in the HSQC spectra are plotted in Figure 7, showing the respective results for heparin-derived octasaccharide, methylated histone peptide, and 25 bp dsDNA. The significant chemical shift perturbations from heparin-derived octasaccharide are mainly located in the N-terminal region and PWWP motif, such that the acidic heparin molecule is aligned on the electropositive interface of protein (Figure 7A). Heparin octasaccharide induced similar perturbation in P24A, and the mutation did not change the perturbation profile. We already knew that methylated histone peptide binds to the aromatic cage of residues Y23, W26, and F49 (Figure 1, red boxes). The addition of H3K36me3 peptide caused chemical shift changes surrounding the PWWP motif and $\beta3-\beta4$ region (Figure 7B). P24A induced similar perturbations in that P24A bound in a manner similar to that observed in HATH. In the titration of DNA, negatively charged DNA induced chemical shift perturbations at the N-terminus, the PWWP motif, and the $\alpha1-\alpha2$ region. Again, the binding profile was similar in the case of P24A. Therefore, the P24A mutation did not show a distinct preference in selecting these interacting targets. We summarize the concentration-dependent chemical shift perturbations in Figure S1 of the Supporting Information.

HATH and P24A in Complex with Long-Chain Heparin and DNA. Under physiological conditions, heparin and DNA molecules are polymers with very large molecular sizes. We examined the binding behaviors of HATHs in complex with long-chain heparin and DNA. We titrated low-molecular-weight heparin (average molecular weight of 30000 Da) and 37 bp dsDNA into HATH and P24A solutions. At low molar ratios, HATH already demonstrated decreased peak intensity in HSQCs because of the increased size of the HATH–ligand complexes (Figure 8). P24A revealed even more significant peak attenuation in response to binding with long-chain DNA (Figure 8A) and heparin (Figure 8B). The peak intensity attenuation reflects the increased size of the complex. Thus, compared to HATH, P24A tended to aggregate or form a larger complex with long-chain DNA and heparin molecules. This result implies stronger intermolecular interaction between P24A units and a possibility of HATH–HATH contact.

Protein–Protein Interaction through the $\beta1-\beta2$ Loop. To ensure the protein–protein contact, we introduced a Cys to replace G22 for the G22C mutation. This position lies at the tip of the $\beta1-\beta2$ loop, near the P24A site. Meanwhile, we mutated C12 to Ser (C12S) to maintain only one Cys residue per HATH unit. We examined the protein–protein contact by monitoring the intermolecular disulfide connectivity. Wild-type HATH and P24A with C12 are less able to form disulfide bond-linked dimers in solution. We tested the new variants of G22C under oxidation conditions (without a reducing agent, β-ME) and reduction conditions (with β-ME). Via sodium dodecyl sulfate–polyacrylamide gel electrophoresis (SDS–PAGE), P24A-C12S/G22C showed a significant population corresponding to a dimeric molecular weight of approximately 30 kDa, whereas HATH-C12S/G22C was less able to form a dimer (Figure 9). The dimers were removed by β-ME, indicating the dimer contained an intermolecular disulfide linkage. The contact between $\beta1-\beta2$ loops allows G22C to incidentally form an intermolecular disulfide bond between the two HATH units. The interaction is more substantial in the P24A variant. In the presence of long-chain DNA and heparin, enhancement of dimer formation was detected in P24A-C12S/G22C as well as HATH-C12S/G22C, and more than 50% of P24A-C12S/G22C was involved in dimers. To test the

DOI: 10.1021/acs.biochem.5b00454
Biochemistry 2015, 54, 4063–4074

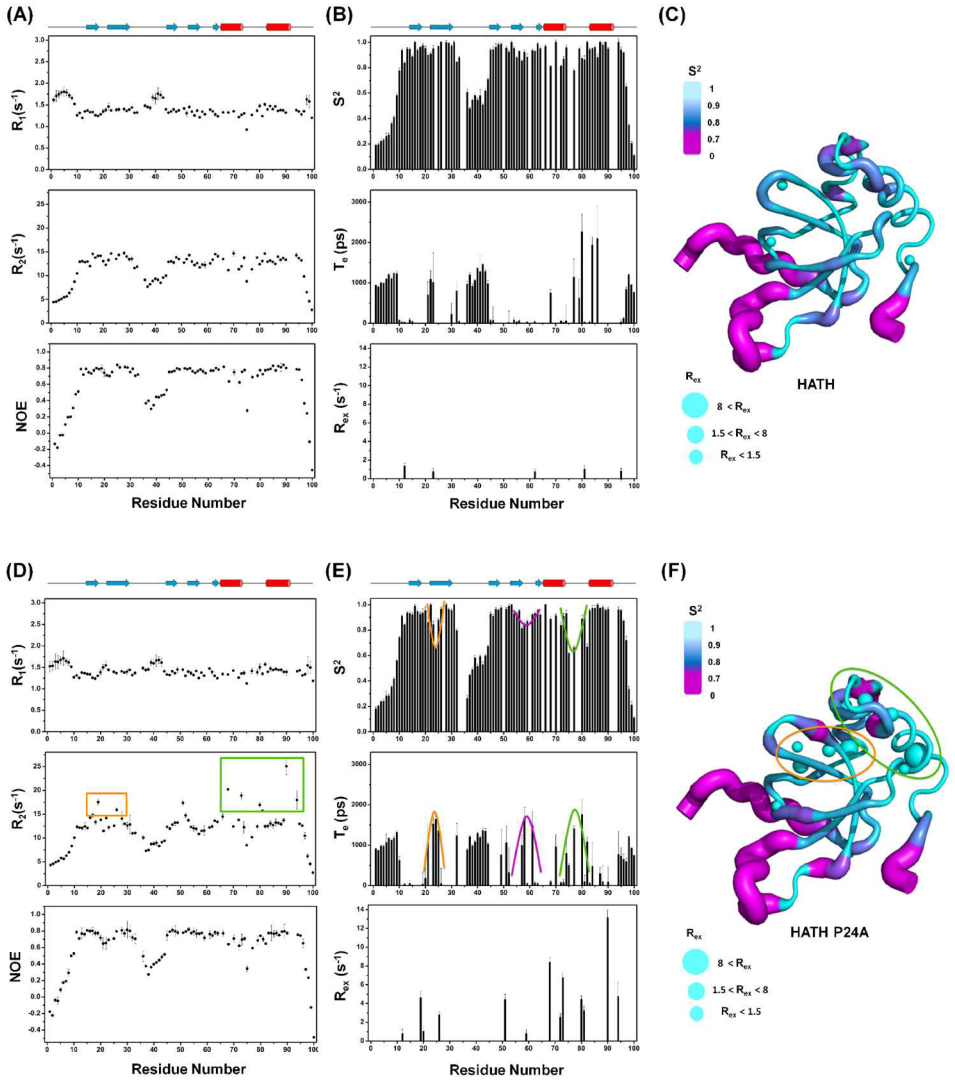

Figure 6. NMR dynamics information of $HATH_{HDGF}$ and the P24A mutant. ^{15}N relaxation parameters (R_1, R_2, and NOE) of (A) HATH and (D) P24A. The perturbations of R_1, R_2, and NOE values are mostly observed in loops and terminal regions. (B and E) Model-free analysis based on the relaxation parameters. Residues with high order parameters ($S^2 > 0.9$) indicate structural rigidity. Residues with observable T_e values exhibit fast motion (picosecond) in solution, whereas residues with R_{ex} perform microsecond to millisecond time scale conformational exchange. (C and F) Structure mapping of the derived dynamics parameters S^2 and R_{ex}. The relaxation data were analyzed using FastModelFree.

specificity of the protein−protein contact, we prepared other mutants of HATH C12S/T55C and HATH C12S/G59C, which were located at β4 and the β4−β5 loop, respectively. Both mutations, unlike G22C, did not induce a greater level of dimer formation (Figure S2 of the Supporting Information). Therefore, the protein−protein contact does not occur randomly through protein aggregation, and the β1−β2 loop is more important for the interaction.

DISCUSSION

We classify HRP HATH domains into A- and P-type HATHs depending on the first residue of the PWWP motif. A-type HATH has the sequence AHWP, and P-type HATH has the sequence PHWP. We mutated the sequence to AHWP in P-type $HATH_{HDGF}$, and the resulting mutant $HATH_{HDGF}$ P24A became less stable, as reflected in the thermal denaturation experiment. The same conclusion is derived for $HATH_{HRP4}$ that the corresponding mutant $HATH_{HRP4}$ A23P is more stable in solution. Thus, the residue type of the first position of the PWWP motif dominantly modulates HATH stability, and the AHWP sequence causes the instability of A-type HATHs.

The HATH domain consists of two structural subdomains, a five-stranded β-barrel in the N-terminus and two α-helices toward the C-terminus. The PWWP motif constitutes part of the β1−β2 region. We inspected the local structure of the PWWP motif and characterized hydrogen bond formation (Figure 10A). In HDGF, the structural elements of β1 and β2 extend to K19 and H25. Two hydrogen bonds are identified between the backbone of A18 and W26. Residue P24 bends the backbone and creates a twist that turns Y23 CO and NH to face the β1 element. This orientation allows Y23 NH to form a hydrogen bond with M20 CO, and the four residues, M20−Y23, constitute a stable β-turn structure. This P-type PWWP motif forms an irregular antiparallel β-structure and creates a β-bulge. Along with another bend created by P27, the β2 element adopts a special orientation to contact the C-terminal helices. All current P-type PWWP domains adopt the loop conformation, including proteins HRP2, HRP3, LEDGF, BRPF1, BRPF2, BRPF3, PDP1, MUM1, and MSH6 (Figure 1).

DOI: 10.1021/acs.biochem.5b00454
Biochemistry 2015, 54, 4063−4074

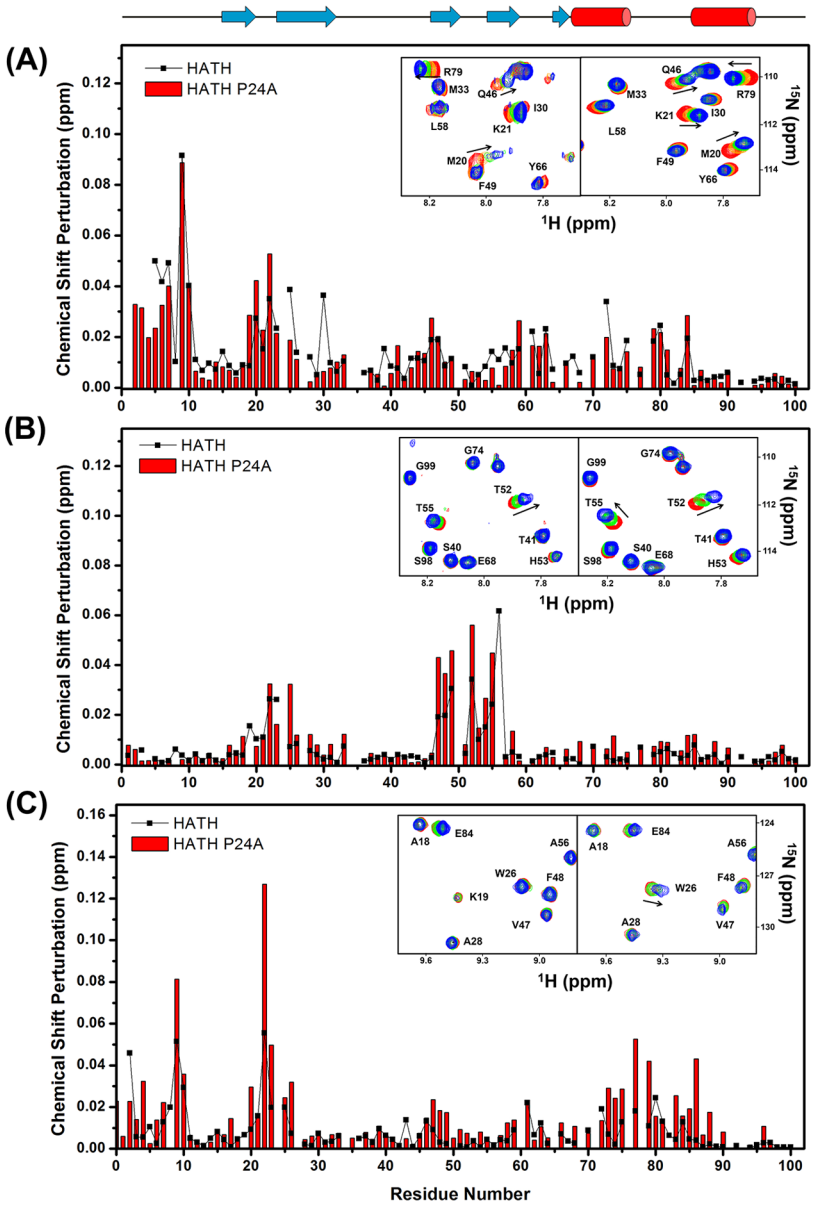

Figure 7. NMR titrations to investigate HATH binding selectivity with various ligands. Combined chemical shift change, $\Delta\delta_{NH+N}$, of $HATH_{HDGF}$ and the P24A mutant induced by (A) heparin octasaccharide in a molar ratio of 1:1, (B) methylated peptide H3K36me3 in a molar ratio of 1:20, and (C) 25 bp dsDNA fragments in a molar ratio of 1:1. The insets show the two-dimensional ^{1}H−^{15}N HSQC spectra of HATH (left) and P24A (right) during titration with ligands from lower to higher ratios colored red, orange, green, and blue.

We noticed that distinct $\beta1-\beta2$ loop conformations occurred in the non-P-type PWWP domains, DNMT3A/DNMT3B and WHSC1L1 (Figure 1). DNMT3A and DNMT3B have the sequence SWWP, and their structures have been determined by X-ray crystallography. We expect similar structural properties between these two proteins because of the conserved sequences. The structure of DNMT3B was determined in the free form (PDB entry 1KHC) and reveals an extended antiparallel β-structure in the $\beta1-\beta2$ loop. An additional hydrogen bond is found between I240 NH and S244 CO (Figure 10B). In two other structures, DNMT3A and DNMT3B bound bis-tris molecules as ligands in their aromatic cages (PDB entries 3LLR and 3QKJ).[7] Interestingly, the binding converts the $\beta1-\beta2$ loop into the loop conformation observed in the P-type PWWP domains. We suspect that the $\beta1-\beta2$ region is structurally flexible in solution, and free DNMT3B was captured in a single conformation during the crystallization process. Upon binding ligands, the flexible $\beta1-\beta2$ loop is stabilized. This idea is partially supported in WHSC1L1. The WHSC1L1 PWWP structure with the sequence RWWP was determined by NMR (PDB entry 2DAQ).[7] Two hydrogen bonds are formed between V17 NH and W25 CO, and the remainder of the loop region is extremely loose, without any defined structure (Figure 10C). This result also indicates the dynamic behavior of the WHSC1L1 $\beta1-\beta2$ loop. As Pro has a fixed backbone conformation, the first Pro in the P-type PWWP domain restricts the structure of the $\beta1-\beta2$ loop. Non-Pro residues have moveable backbone dihedral angles, which introduce flexibility into the loop. This difference explains the structural instability occurring in the A-type HATHs.

In the P24A mutant, the NMR H/D experiment reported decreased structural stability throughout the entire protein. The change in the PWWP motif affects the C-terminal helices. The

DOI: 10.1021/acs.biochem.5b00454
Biochemistry 2015, 54, 4063−4074

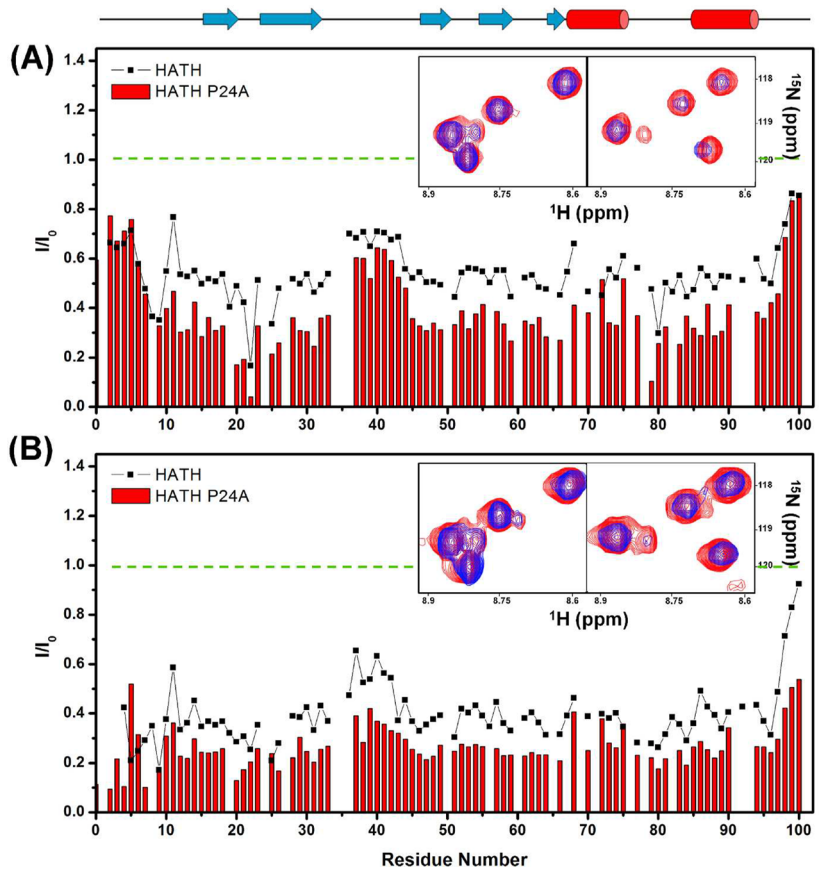

Figure 8. NMR titrations to investigate HATH aggregation property with long-chain DNA and heparin. Peak intensity attenuation (I/I_0) of HATH and P24A (A) induced by 37 bp dsDNA at a 1:0.2 protein:DNA molar ratio and (B) induced by heparin polysaccharide at a 1:0.1 protein:heparin molar ratio. The insets show the two-dimensional $^{1}H-^{15}N$ HSQC spectra of HATH (left) and P24A (right) during titration. Spectra of free and bound forms are colored red and blue, respectively.

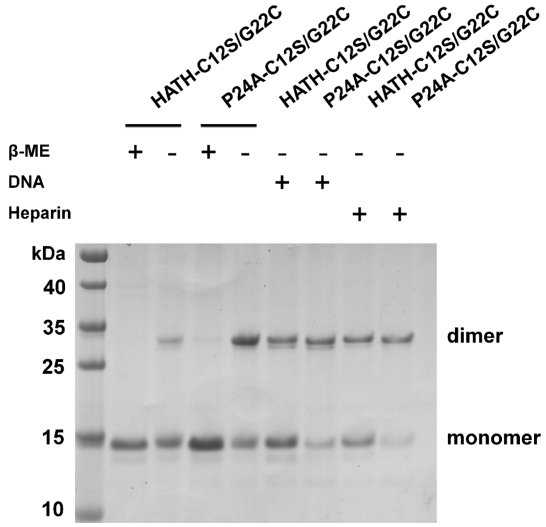

Figure 9. SDS–PAGE assay of HATH variants of HATH-C12S/G22C and P24A-C12S/G22C under reduction conditions (with β-ME) and oxidation conditions (without β-ME). The two major bands correspond to monomer and disulfide bond-linked dimer of HATH variants. DNA and heparin oligomers promote dimer formation in both HATH-C12S/G22C and P24A-C12S/G22C, and P24A-C12S/G22C showed better dimerization ability.

PWWP motif constitutes the N-terminal part of β2 that is adjacent to the C-terminal C-helices. The PWWP motif provides hydrophobic contact between the β-barrel and the α1 and α2 elements. Local hydrophobic and aromatic residues such as H25, W26, P27, F73, F82, and L86 contribute to the interaction. Through this structural contact, the PWWP motif affects the dynamics and stability of C-terminal helices. R_1, R_2, and heteronuclear NOE measurements support the same conclusion: there exists synchronized molecular dynamics between the mutation site and the region near residues 70–85, such that T_e, R_{ex}, and reduced S^2 values were spontaneously observed in the two regions of the P24A mutant. P24A introduced higher backbone flexibility and conformational exchange. Thus, the PWWP motif acts as an important structural motif in supporting C-terminal helices, and the P24A mutation changes the overall structural properties of the HATH domain, from the β-barrel to the C-terminal helices.

We evaluated the interactions of this structurally unstable mutation with the ligands to assist in understanding the functional difference between A- and P-type HATHs. The HATH domain recognizes heparin and DNA fragments through its electropositive surface and recognizes H3K36me3 peptide through its conserved aromatic cage. Surprisingly, the chemical shift perturbations induced by the three ligands were similar in the two HATHs (Figure 7), and the binding affinities determined from the NMR titration experiments were also similar. The dramatic difference is derived from the binding with long-chain ligands (heparin polysaccharide and 37 bp dsDNA), which induced more significant NMR line broadening in P24A (Figure 8). The effect might be correlated with the

DOI: 10.1021/acs.biochem.5b00454
Biochemistry 2015, 54, 4063–4074

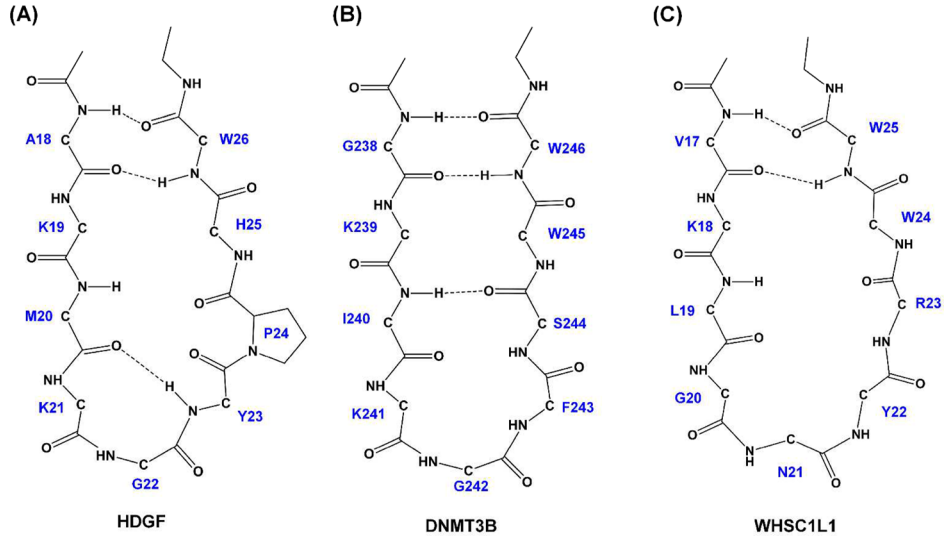

Figure 10. Classification of PWWP domains based on hydrogen bond formation in the $\beta1-\beta2$ loop. Three examples are compared: (A) HDGF, (B) DNMT3B, and (C) WHSC1L1.

P24A aggregation property. However, we identified the specific contact between $\beta1-\beta2$ loops, as demonstrated by the enhanced population of the P24A-C12S/G22C dimer via SDS–PAGE (Figure 9). We therefore propose a mechanism that P24A can easily form a larger complex with polymer ligands. A flexible $\beta1-\beta2$ loop creates better contact between the two HATH units, which means that A-type HATH favors such interaction. This model is supported by the newly released WHSC1L1 PWWP structure, in which the PWWP domain contains a longer C-terminal helix, and two WHSC1L1 molecules pack in one crystal unit (PDB entry 4RXJ). The $\beta1-\beta2$ loops contact each other in the structure and act as part of the dimer interface. Nevertheless, the ability of A-type HATH to coordinate two proximate polymer chains to form a superstructure could be of significance, for example, in forming a protein–carbohydrate complex for receptor recognition in the extracellular matrix and a protein–DNA complex for DNA packing in the nucleosome.

In conclusion, the first residue of the PWWP motif affects the HATH domain stability because a Pro residue creates a unique β-bulge structure in the $\beta1-\beta2$ region. Although the stability of the HATH domain does not correlate to ligand binding selectivity, it modulates protein–protein contact through the $\beta1-\beta2$ loop. A-type HATH exhibits lower protein stability but a stronger tendency to form aggregations in solution. We suggest a molecular model in which HATH domain exhibits ability for forming a larger complex when binding DNA and heparin polymers.

■ ASSOCIATED CONTENT

Supporting Information

NMR titration curves of $HATH_{HDGF}$ and $HATH_{HDGF}$ P24A residues (Figure S1) and SDS–PAGE assay of HATH variants (Figure S2). The Supporting Information is available free of charge on the ACS Publications website at DOI: 10.1021/acs.biochem.5b00454.

■ AUTHOR INFORMATION

Corresponding Author

*Institute of Bioinformatics and Structural Biology, National Tsing Hua University, Hsinchu, Taiwan. E-mail: scsue@life.nthu.edu.tw. Telephone: (886)-3-5742025. Fax: (886)-3-5715934.

Funding

This work was supported by the Ministry of Science and Technology (MOST), Taiwan (101-2311-B-007-013, 101-2311-B-009-006-MY2, and 103-2627-M-007-007), and National Tsing Hua University (104N2051E1).

Notes

The authors declare no competing financial interest.

■ ACKNOWLEDGMENTS

We are grateful to the National Synchrotron Radiation Research Center for CD measurement, the NMR facility at National Tsing Hua University, and the Core Facility for Protein Structural Analysis at Academia Sinica for NMR measurements.

■ REFERENCES

(1) Stec, I., Nagl, S. B., van Ommen, G. J., and den Dunnen, J. T. (2000) The PWWP domain: A potential protein-protein interaction domain in nuclear proteins influencing differentiation? *FEBS Lett. 473*, 1–5.

(2) Qin, S., and Min, J. (2014) Structure and function of the nucleosome-binding PWWP domain. *Trends Biochem. Sci. 39*, 536–547.

(3) Stec, I., Wright, T. J., van Ommen, C. J. B., de Boer, P. A. J., van Haeringen, A., Moorman, A. F. M., Altherr, M. R., and den Dunnen, J. T. (1998) WHSC1, a 90 kb SET domain-containing gene, expressed in early development and homologous to the Drosophila dysmorphy gene maps in the Wolf-Hirschhorn syndrome critical region and is fused to IgH in t(4;14) multiple myeloma (vol 7, pg 1071, 1998). *Hum. Mol. Genet. 7*, 1527–1528.

(4) Sue, S. C., Chen, J. Y., Lee, S. C., Wu, W. G., and Huang, T. H. (2004) Solution structure and heparin interaction of human hepatoma-derived growth factor. *J. Mol. Biol. 343*, 1365–1377.

(5) Chen, F.-F., Lin, W.-H., Lin, S.-C., Kuo, J.-H., Chu, H.-Y., Huang, W.-C., Chuang, Y.-J., Lee, S.-C., and Sue, S.-C. (2012) Significance of heparin binding to basic residues in homologous to the amino terminus of hepatoma-derived growth factor and related proteins. *Glycobiology 22*, 649–661.

(6) Lukasik, S. M., Cierpicki, T., Borloz, M., Grembecka, J., Everett, A., and Bushweller, J. H. (2006) High resolution structure of the

DOI: 10.1021/acs.biochem.5b00454
Biochemistry 2015, 54, 4063–4074

HDGF PWWP domain: A potential DNA binding domain. *Protein Sci. 15*, 314−323.
(7) Wu, H., Zeng, H., Lam, R., Tempel, W., Amaya, M. F., Xu, C., Dombrovski, L., Qiu, W., Wang, Y., and Min, J. (2011) Structural and histone binding ability characterizations of human PWWP domains. *PLoS One 6*, e18919.
(8) Qiu, C., Sawada, K., Zhang, X., and Cheng, X. (2002) The PWWP domain of mammalian DNA methyltransferase Dnmt3b defines a new family of DNA-binding folds. *Nat. Struct. Mol. Biol. 9*, 217−224.
(9) Slater, L. M., Allen, M. D., and Bycroft, M. (2003) Structural variation in PWWP domains. *J. Mol. Biol. 330*, 571−576.
(10) Ikegame, K., Yamamoto, M., Kishima, Y., Enomoto, H., Yoshida, K., Suemura, M., Kishimoto, T., and Nakamura, H. (1999) A new member of a hepatoma-derived growth factor gene family can translocate to the nucleus. *Biochem. Biophys. Res. Commun. 266*, 81−87.
(11) Kishima, Y., Yamamoto, H., Izumoto, Y., Yoshida, K., Enomoto, H., Yamamoto, M., Kuroda, T., Ito, H., Yoshizaki, K., and Nakamura, H. (2002) Hepatoma-derived growth factor stimulates cell growth after translocation to the nucleus by nuclear localization signals. *J. Biol. Chem. 277*, 10315−10322.
(12) Wang, C. H., Davamani, F., Sue, S. C., Lee, S. C., Wu, P. L., Tang, F. M., Shih, C., Huang, T. H., and Wu, W. G. (2011) Cell surface heparan sulfates mediate internalization of the PWWP/HATH domain of HDGF via macropinocytosis to fine-tune cell signalling processes involved in fibroblast cell migration. *Biochem. J. 433*, 127−138.
(13) Dhayalan, A., Rajavelu, A., Rathert, P., Tamas, R., Jurkowska, R. Z., Ragozin, S., and Jeltsch, A. (2010) The Dnmt3a PWWP domain reads histone 3 lysine 36 trimethylation and guides DNA methylation. *J. Biol. Chem. 285*, 26114−26120.
(14) Chiu, L.-Y., Hung, K.-W., Tjong, S.-C., Chiang, Y.-W., and Sue, S.-C. (2014) NMR characterization of the electrostatic interaction of the basic residues in HDGF and FGF2 during heparin binding. *Biochim. Biophys. Acta 1844*, 1851−1859.
(15) Eidahl, J. O., Crowe, B. L., North, J. A., McKee, C. J., Shkriabai, N., Feng, L., Plumb, M., Graham, R. L., Gorelick, R. J., and Hess, S. (2013) Structural basis for high-affinity binding of LEDGF PWWP to mononucleosomes. *Nucleic Acids Res. 41*, 3924−3936.
(16) Yu, Q., Wen, Z., Chen, Z., Yan, W., Weiwei, W., Jiahai, Z., Zhiyong, Z., Guohong, L., Yunyu, S., and Xiaoming, T. (2012) Solution structure of the Pdp1 PWWP domain reveals its unique binding sites for methylated H4K20 and DNA. *Biochem. J. 442*, 527−538.
(17) Musselman, C. A., Gibson, M. D., Hartwick, E. W., North, J. A., Gatchalian, J., Poirier, M. G., and Kutateladze, T. G. (2013) Binding of PHF1 Tudor to H3K36me3 enhances nucleosome accessibility. *Nat. Commun. 4*, 2969.
(18) Yang, J., and Everett, A. D. (2007) Hepatoma derived growth factor binds DNA through the N-terminal PWWP domain. *BMC Mol. Biol. 8*, 101.
(19) Jia, D., Jurkowska, R. Z., Zhang, X., Jeltsch, A., and Cheng, X. (2007) Structure of Dnmt3a bound to Dnmt3L suggests a model for de novo DNA methylation. *Nature 449*, 248−251.
(20) van Nuland, R., van Schaik, F., Simonis, M., van Heesch, S., Cuppen, E., Boelens, R., Timmers, H. M., and van Ingen, H. (2013) Nucleosomal DNA binding drives the recognition of H3K36-methylated nucleosomes by the PSIP1-PWWP domain. *Epigenet. Chromatin 6*, 12.
(21) Min, J., Allali-Hassani, A., Nady, N., Qi, C., Ouyang, H., Liu, Y., MacKenzie, F., Vedadi, M., and Arrowsmith, C. H. (2007) L3MBTL1 recognition of mono-and dimethylated histones. *Nat. Struct. Mol. Biol. 14*, 1229−1230.
(22) Kalakonda, N., Fischle, W., Boccuni, P., Gurvich, N., Hoya-Arias, R., Zhao, X., Miyata, Y., Macgrogan, D., Zhang, J., and Sims, J. (2008) Histone H4 lysine 20 monomethylation promotes transcriptional repression by L3MBTL1. *Oncogene 27*, 4293−4304.
(23) Vezzoli, A., Bonadies, N., Allen, M. D., Freund, S. M., Santiveri, C. M., Kvinlaug, B. T., Huntly, B. J., Göttgens, B., and Bycroft, M. (2010) Molecular basis of histone H3K36me3 recognition by the PWWP domain of Brpf1. *Nat. Struct. Mol. Biol. 17*, 617−619.
(24) Dietz, F., Franken, S., Yoshida, K., Nakamura, H., Kappler, J., and Gieselmann, V. (2002) The family of hepatoma-derived growth factor proteins: Characterization of a new member HRP-4 and classification of its subfamilies. *Biochem. J. 366*, 491−500.
(25) Enomoto, H., Yoshida, K., Kishima, Y., Kinoshita, T., Yamamoto, M., Everett, A. D., Miyajima, A., and Nakamura, H. (2002) Hepatoma-derived growth factor is highly expressed in developing liver and promotes fetal hepatocyte proliferation. *Hepatology 36*, 1519−1527.
(26) Kishima, Y., Yoshida, K., Enomoto, H., Yamamoto, M., Kuroda, T., Okuda, Y., Uyama, H., and Nakamura, H. (2002) Antisense oligonucleotides of hepatoma-derived growth factor (HDGF) suppress the proliferation of hepatoma cells. *Hepatogastroenterology 49*, 1639−1644.
(27) Hu, T. H., Huang, C. C., Liu, L. F., Lin, P. R., Liu, S. Y., Chang, H. W., Changchien, C. S., Lee, C. M., Chuang, J. H., and Tai, M. H. (2003) Expression of hepatoma-derived growth factor in hepatocellular carcinoma. *Cancer 98*, 1444−1456.
(28) Abouzied, M. M., Baader, S. L., Dietz, F., Kappler, J., Gieselmann, V., and Franken, S. (2004) Expression patterns and different subcellular localization of the growth factors HDGF (hepatoma-derived growth factor) and HRP-3 (HDGF-related protein-3) suggest functions in addition to their mitogenic activity. *Biochem. J. 378*, 169−176.
(29) Everett, A. D., Yang, J., Rahman, M., Dulloor, P., and Brautigan, D. L. (2011) Mitotic phosphorylation activates hepatoma-derived growth factor as a mitogen. *BMC Cell Biol. 12*, 15.
(30) Abouzied, M. M., El-Tahir, H. M., Gieselmann, V., and Franken, S. (2010) Hepatoma-derived growth factor-related protein-3: A new neurotrophic and neurite outgrowth-promoting factor for cortical neurons. *J. Neurosci. Res. 88*, 3610−3620.
(31) Wu, X., Daniels, T., Molinaro, C., Lilly, M., and Casiano, C. (2002) Caspase cleavage of the nuclear autoantigen LEDGF/p75 abrogates its pro-survival function: Implications for autoimmunity in atopic disorders. *Cell Death Differ. 9*, 915−925.
(32) Zhang, J., Ren, H., Yuan, P., Lang, W., Zhang, L., and Mao, L. (2006) Down-regulation of hepatoma-derived growth factor inhibits anchorage-independent growth and invasion of non-small cell lung cancer cells. *Cancer Res. 66*, 18−23.
(33) Yoshida, K., Nakamura, H., Okuda, Y., Enomoto, H., Kishima, Y., Uyama, H., Ito, H., Hirasawa, T., Inagaki, S., and Kawase, I. (2003) Expression of hepatoma-derived growth factor in hepatocarcinogenesis. *J. Gastroenterol. Hepatol. 18*, 1293−1301.
(34) Matsuyama, A., Inoue, H., Shibuta, K., Tanaka, Y., Barnard, G. F., Sugimachi, K., and Mori, M. (2001) Hepatoma-derived growth factor is associated with reduced sensitivity to irradiation in esophageal cancer. *Cancer Res. 61*, 5714−5717.
(35) Delaglio, F., Grzesiek, S., Vuister, G. W., Zhu, G., Pfeifer, J., and Bax, A. (1995) NMRPipe: A multidimensional spectral processing system based on UNIX pipes. *J. Biomol. NMR 6*, 277−293.
(36) Goddard, T. D., and Kneller, D. G. *SPARKY 3*, University of California, San Francisco.
(37) Cole, R., and Loria, J. P. (2003) FAST-Modelfree: A program for rapid automated analysis of solution NMR spin-relaxation data. *J. Biomol. NMR 26*, 203−213.
(38) Tjandra, N., Feller, S. E., Pastor, R. W., and Bax, A. (1995) Rotational diffusion anisotropy of human ubiquitin from ^{15}N NMR relaxation. *J. Am. Chem. Soc. 117*, 12562−12566.
(39) Huang, Y.-T., Liaw, Y.-C., Gorbatyuk, V. Y., and Huang, T.-H. (2001) Backbone dynamics of *Escherichia coli* thioesterase/protease I: Evidence of a flexible active-site environment for a serine protease. *J. Mol. Biol. 307*, 1075−1090.
(40) Hiyama, Y., Niu, C. H., Silverston, J. V., Bavavo, A., and Torchia, D. A. (1988) Determination of ^{15}N chemical shift tensor *via* ^{15}N-^{2}H dipolar coupling in Bocglycylglycyl[^{15}N] glycine benzyl ester. *J. Am. Chem. Soc. 110*, 2378−2383.

DOI: 10.1021/acs.biochem.5b00454
Biochemistry 2015, 54, 4063−4074

(41) Lipari, G., and Szabo, A. (1982) Model-free approach to the interpretation of nuclear magnetic resonance relaxation in macromolecules. 1. Theory and range of validity. *J. Am. Chem. Soc. 104*, 4546−4559.
(42) Englander, S. W., Sosnick, T. R., Englander, J. J., and Mayne, L. (1996) Mechanisms and uses of hydrogen exchange. *Curr. Opin. Struct. Biol. 6*, 18−23.

DOI: 10.1021/acs.biochem.5b00454
Biochemistry 2015, 54, 4063−4074